

Sensing Local Geometry for Dexterous Manipulation

William R. Provancher and Mark R. Cutkosky

Center for Design Research, Stanford University
Stanford, California 94305-2232

wil@cdr.stanford.edu; <http://www-cdr.stanford.edu/telem nip>

Abstract: We describe a new tactile sensor for use in dexterous manipulation and telemanipulation. The sensor consists of an array of curvature-measuring elements embedded in a compliant membrane. The resulting sensor is inexpensive and robust, and can be used in robotic hands with soft fingertips for object handling and exploration. The curvature measurements provide information for manipulation planning and control and provide an estimate of the local object geometry, useful for grasp stability analysis. The prototype device consists of an array of strain gages fabricated within a compliant membrane. Object curvature estimation results are presented, along with suggestions for improvements in future versions of the device.

1. INTRODUCTION

Dexterous manipulation in humans and in robots requires information about the contact conditions between the fingertips and a grasped object. For example, when rolling an object between the fingertips, the curvature of the object and the locations of contacts on the finger and object surfaces must be known to plan the required finger motions. Other surface properties such as friction and compliance also influence the manipulation strategy. In humans, such information is obtained through a combination visual and tactile sensing and is essential for skillful object handling.

In robots, despite many years of research, the state of the art in tactile sensing and interpretation is comparatively primitive. The challenge of creating a sensate artificial "skin" for robotic hands is formidable. Trade-offs must inevitably be made among spatial resolution, robustness, pressure sensitivity and the ability to comply with irregular or curved surfaces. Providing power and transporting signals along the robot fingers are also difficult, especially when the digits are human-sized or smaller. Nonetheless, many kinds of tactile sensors have been reported in the literature. For reviews of the state of the art in robotic tactile sensing see (Dario 1991) and (Lee 2000).

In most implementations, the tactile sensors consist of an array of pressure or pressure and shear-sensing elements. The compliance of these sensors can be tailored but, in general, cannot accommodate large deformations. However, other researchers starting with Broukett (1985) have argued the merits of soft robotic

fingertips consisting of a skin covering an inner layer of liquid or foam. With these sensors, it becomes more practical to measure deformations of the skin rather than pressure and shear stress distributions. Nowlin (1991), Russel (1992) and Ferrier and Brocket (2000) present tactile sensors of this type. The salient characteristic of these sensors is that they measure deflections of the skin and, with suitable processing, can provide measurements of local object geometry. Thus, in addition to the practical advantages afforded by soft fingertips, they provide information that is of direct use for planning dexterous motions with rolling and/or sliding. A difficulty with previous soft-finger designs, however, is that they pose challenging numerical problems to reconstruct the skin geometry from (noisy) sensor readings.

The following sections present the conceptual approach, the sensor design and construction, and the results of simulations and experiments. We conclude with a discussion of the results and our recommendations for future work.

2. SHAPE SENSING APPROACH

This section describes our general approach for measuring robot fingertip geometry (and by inference, local object geometry) using an array of curvature measuring elements.

2.1 Sensor Concept

The sensing approach is compatible with a soft skin covering a layer of foam or fluid (Fig. 1) and allows the skin geometry to be reconstructed with a minimum of computation. For measuring local object geometry we consider a curved patch, as shown in Fig 2. We measure the surface patch at $(n \times m)$ points resulting in an array of curvature information (principal curvatures and torsion) (Montana 1988). The shape of the patch is obtained by matching curvatures of the basis functions and satisfying boundary conditions.

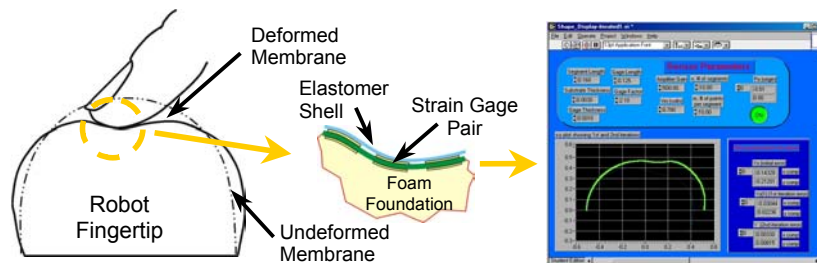


Fig. 1. Schematic of sensor construction and typical results for a linear sensor prototype

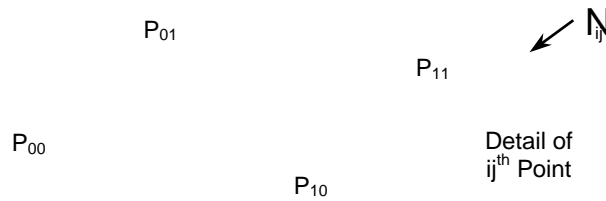


Fig. 2. General (n x m) parametric surface patch. Detail of local surface shows curvature sensing element N_{ij} which indicates curvature of the ij^{th} point

2.2 Data Fitting

The curved membrane resembles a deforming drum head and its surface can be represented by a two-dimensional Fourier sine series.

$$f = \sum_i c_{ij} \sin i \pi x \sin j \pi y ; \quad i = 1:N, \quad j = 1:N \quad (1)$$

In this example, the Fourier series is chosen so all terms are identically zero at $x = 0$ and 1 , and $y = 0$ and 1 , corresponding to a square membrane. Similar representations can be used for other shapes.

The standard least squares procedure is reused to solve for the Fourier coefficients. The measurements are reported by the following matrix equation:

$$M \tilde{c} = K \quad (2)$$

where K is the $(N_x \times N_y \times 3)$ vector of curvature measurements, M is the $(N_x \times N_y \times 3 \times N_c)$ measurement matrix, and \tilde{c} is the $(N_c \times 1)$ vector of Fourier coefficients. Measurements are taken over an unrectangular grid of points. The total number of measurements is three times the number of grid points $(3N_x N_y)$ because three scalar curvature measurements are made at each grid point. The curvature measurements N_x , N_y , and N_z are related to the surface deformation by the following equations:

$$N_{xx} = \frac{\partial^2 f}{\partial x^2} \quad N_{yy} = \frac{\partial^2 f}{\partial y^2} \quad N_{xy} = \frac{\partial^2 f}{\partial x \partial y} \quad (3,4,5)$$

The standard least squares procedure gives the following estimate for the Fourier coefficients using the Moore-Penrose Left Pseudo inverse:

$$c = (M^T M)^{-1} M^T K \quad (6)$$

2.3 Sensor Design

The sensor design employs a standard method for measuring bending strain, placing pairs of gages back-to-back and wiring these gages in a half-bridge configuration. Strain gages are well characterized and known to follow the relationship: $\Delta R/R_g = GF \epsilon$ where R_g is the gage resistance before strain is applied, ΔR is the change in resistance to an applied strain ϵ , and G is the strain applied.

to the gage and GF is the gage factor. The resulting signals are proportional to the average radius of curvature the gages (see Eqs. (7) and (8) which follow). Other benefits to this gage configuration include temperature compensation and segregation of axial strains (Fraden 1996).

The output voltage, V_{out} , is represented by the following equation:

$$V_{out} = V_{in} GF (t_s + t_g) Gain / (4 R_m) \quad (7)$$

where V_{in} is the bridge excitation voltage, R_m is the mean radius of curvature of the membrane centerline, t_s is the thickness of the membrane substrate, t_g is the gage thickness and “Gain” is the bridge amplification. Eq. (7) can be rearranged in terms of average curvature, κ , where curvature can be shown as the reciprocal of radius of curvature and $\kappa(i)$ represents the curvature of the i th gage pair.

$$\kappa(i) = 1/R_m = 4V_{out} / [V_{in} GF (t_s + t_g) Gain] \quad (8)$$

The sensor was designed to stay within the elastic limits of the metal foil strain gages (about 1% strain).

3. SENSOR CONSTRUCTION

The first prototype array was built in halves by bonding commercially available strain gage arrays to a custom-fabricated polyimide flex circuit. Electrical junctions between the flex circuit and strain gages were made using solder paste and 13 μm thick copper foil to maintain thin sensor profile. The two halves are bonded together using acrylic PSA film adhesive (Fig. 3).

The sensor electronics are comprised of the multiplexed strain gage half-bridges balanced by a dummy half-bridge and amplified by a commercial instrumentation amplifier (Fig. 4). R_d is the resistance of the bridge dummy resistor, R_g is the resistance of the active gages and V_{bal} is the nominal voltage of a dummy half-bridge required to balance the circuit.

A second generation prototype shown in Fig. 5 includes local multiplexing, amplification and signal conditioning using surface mount devices on the same flexible circuit that supports the strain gages.

4. SIMULATION RESULTS FOR DATA FITTING

A numerical simulation was conducted to determine the effects in position space of fitting to a surface in curvature space, and to characterize the effects of sensor noise on reconstruction.

The first step in validation is to generate a reference surface chosen to approximate some expected load. It is convenient if this reference surface can be approximated by a continuous function $f(x,y)$ that permits direct calculation of simulated curvature data (κ_{xx} , κ_{yy} and κ_{xy}). Timoshenko and Gere (1961) present such a solution for deformations of a thin plate due to an arbitrary point load. The solution in Eq. (9), which describes the displacements in the z -direction as a

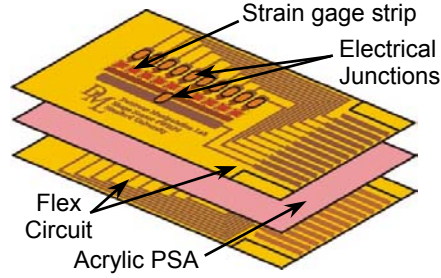


Fig. 3. Sensor array construction for the first-generation prototype

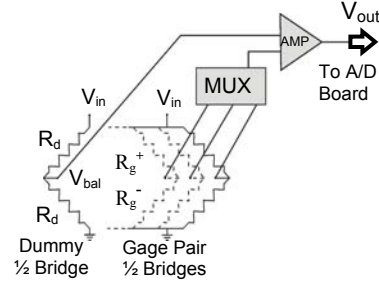


Fig. 4. Sensor array electrical schematic

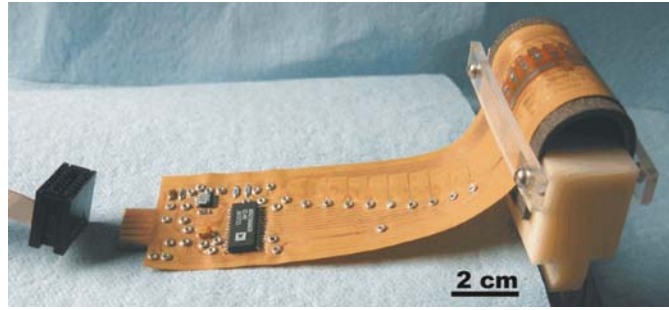


Fig. 5. Second generation sensor with integral multiplexing and signal conditioning

function of x and y , is represented as a two-dimensional Fourier sine series similar to that shown in Eq. (1) for the basis functions:

$$w = \sum a_{ij} \sin(i\pi x) \cdot \sin(j\pi y) \quad (9)$$

$$\text{where } a_{ij} = \frac{4 \cdot Q \cdot \sin(i\pi\xi) \cdot \sin(j\pi\eta)}{D\pi^4(i^2 + j^2)^2};$$

ξ, η are the x, y coordinates of load Q

D is the flexural rigidity of the plate, $D = E \cdot h^3 / 12(1 + \nu^2)$;

E is Young's Modulus, h is the plate thickness, ν is Poisson's ratio

More complex load cases can be represented through superposition of several point loads.

For simulation, three load cases were considered: (1) a centered point load ($\xi = 0.5, \eta = 0.5$); (2) an off-center point load ($\xi = 0.2, \eta = 0.8$); and (3) a skewed line load (from $\xi = 0.1, \eta = 0.9$ to $\xi = 0.9, \eta = 0.1$). Simulated curvature data were produced by taking appropriate derivatives of the reference surface displacement function. To simulate the effects of sensor noise on the reconstruction, random noise, with RMS value of $\Delta\kappa = 0.23 \text{ m}^{-1}$ (approximately 25% of the average curvature values) and a maximum value of $\Delta\kappa = 0.40 \text{ m}^{-1}$, was

added to the simulated curvature data. The basis functions were fit directly to the simulated curvature data. The “truth” model for the two-dimensional surface was represented by a two-dimensional (15×15) Fourier series. There were 100 measurement points (10×10) with three measurements at each point for a total of 300 measurements. The fitted model had 64 parameters (8×8) Fourier coefficients.

The quality of data fitting was quantified by recording the maximum calculated displacement, w_{Max} , at the point of load application and the distributed RMS error, $E_{w,RMS}$, relative to the reference surface. The first metric was chosen because of its significance to manipulation kinematics. During manipulation, the point of load application is the same as with the object contact point and small deformations at the robot fingertip ultimately effect the precision of fine manipulations. Table 1 reports the maximum calculated displacement at the point of load application, w_{Max} , the absolute error of this displacement, $E_{w,Max}$, and the RMS error for the entire surface, $E_{w,RMS}$, as compared to the reference surface. Fig. 6 shows typical mesh plots of simulation results. Similar results were also determined for the one-dimensional simulation of a planar curve and in the following section the planar curve simulation results are compared with experimental results.

5. EXPERIMENTS

To confirm sensor operation before embedding in a robot fingertip, the sensor was calibrated against cylindrical objects of known curvature. For these objects, one would expect the sensor output to be directly proportional to object curvature. This was confirmed for objects with small curvature. However, testing of a first-generation sensor revealed hysteresis, traced to creep in the acrylic film adhesive.

A second-generation prototype was fabricated in which the strain gages are bonded directly to a two-sided flex circuit of $25 \mu\text{m}$ polyimide clad with $35 \mu\text{m}$ thick copper on both sides. The pattern was created using standard positive photoresist technology. In addition, the second-generation prototype includes local sensor electronics on the same flexible circuit that supports the strain gages (Fig. 5). Despite these improvements, the sensor still exhibits some mechanical

Table 1. Simulation results for a 10cm x 10cm surface patch with a 10 x 10 array of curvature measuring elements subjected to various load conditions

Load Case	Max Displacement		Error	RMS Error	
	$w_{Applied}$ [mm]	w_{Max} [mm]	$E_{w,Max}$ [mm]	$E_{w,RMS}$ [mm]	
Centered Point Load ($\xi = .5, \eta = .5$)	4.70	(no noise)	4.59	-0.11	0.067
		(w/ noise)	4.98	-0.12	0.083
Off-center Point Load ($\xi = .2, \eta = .8$)	4.89	(no noise)	4.58	-0.31	0.316
		(w/ noise)	4.56	0.34	0.317
Skewed Line Load ($\xi = .1, \eta = .9$ to $\xi = .9, \eta = .1$)	4.68	(no noise)	4.63	-0.05	0.193
		(w/ noise)	4.62	-0.06	0.191

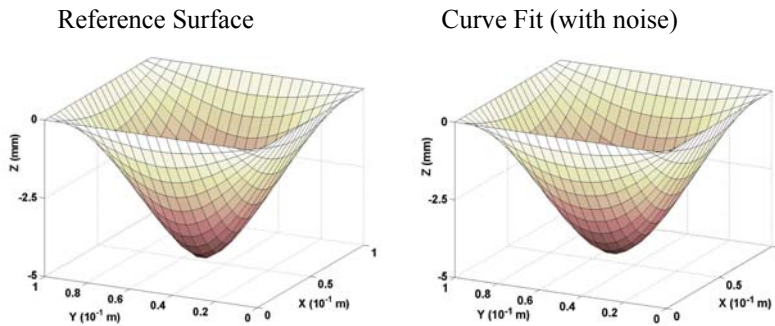


Fig. 6. Mesh plots showing typical simulation results for the case of a centered point load. The reference surface is shown on the left and the surface fit to data with simulated noise on the right

hysteresis. To quantify the hysteresis, measurements were made against a sequence of objects of known curvature as shown in Fig. 7. Data were recorded starting with objects of large radius of curvature (small curvature) and progressing to objects of decreasing radius of curvature and back again to larger objects. The sensor was then flipped over and measurements of objects were made with the opposite face of the sensor in contact with objects, again starting with large objects and progressing as described above. Each gage pair of the sensor was calibrated over the range of measurements taken during the above procedure. Calibration consisted of standard least squares fitting of curvature data. Results of the hysteresis test (and calibration) are shown in Fig. 8.

A simple test configuration was chosen to validate the sensor concept experimentally. The sensor was tested as it would be used on a cylindrical robot fingertip (Fig. 5). A centered line load was applied to the sensor, indicated as “Q”



Fig. 7. First-generation sensor calibrated using objects of known curvature

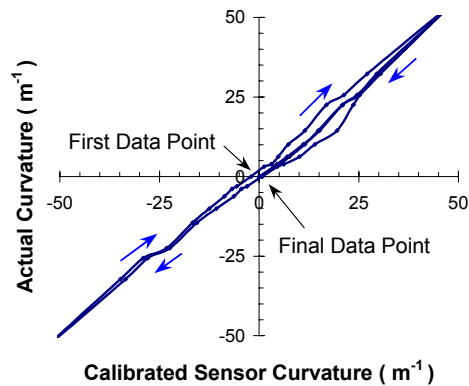


Fig. 8. Sensor calibration data for second generation strain gage array prototype. Some hysteresis is evident as shown by the loop

in Fig. 9. For this type of loading, the sensor deforms as a curved beam of radius, $R_0 = 12.9$ mm. Expected radial deflections, u , of the sensor can be calculated using a standard Rayleigh-Ritz approximation (in polar coordinates):

$$u = a_0(\sin(\theta) + 3 \cdot \cos(\theta)); \text{ for } \theta = 0 \text{ to } \pi, \quad (10)$$

$$\text{where } a_0 = -Q \cdot R_0^3 / 72\pi \cdot EI$$

The curvature at each point is given by:

$$\kappa_\theta \approx (1/R_0^2) \partial^2 u / \partial \theta^2 + (1/R_0) u \quad (11)$$

The experimental results are compared with equivalent simulation results for planar curve as shown in Table 2. For each applied load, the center deflection, u_{Max} , of the sensor was recorded for three discrete load cases of increasing magnitude ($u_{\text{Applied}} = 0.63$ mm, 1.27 mm and 1.90 mm). The simulation has knowledge of the entire reference curve geometry, but the experiment only has knowledge of the displacement at the point of load application. Therefore, the quality of data fitting for the experiments was quantified by recording the maximum calculated displacement, u_{Max} , at the point of load application while maintaining a reasonable curve shape. For both the experimental and simulation results there were 10 curvature measurements, one at each of 10 data points. The “truth” model for the simulation was represented by Eq. (10). The fitted model had 8 parameters (8 Fourier coefficients). Table 2 reports the maximum calculated displacement at the point of load application, u_{Max} , as well as the absolute error of this displacement, $E_{u,\text{Max}}$, compared to the applied displacement, u_{Applied} . Results are plotted in Fig. 9.

6. DISCUSSION AND CONCLUSIONS

6.1 Simulation Results

The numerical simulation results show that a series of discrete curvature measurements can be used to obtain a reasonably accurate reconstruction of the

Table 2. Experimental and simulation results for centered loaded sensor. Results are presented for increasing magnitude of center deflection

Load Case	Applied Displcmt. u_{Applied} [mm]	Experimental Results		Simulation Results (w/ noise*)		
		u_{Max} [mm]	Error	u_{Max} [mm]	Error	RMS Error
			$E_{u,\text{Max}}$ [mm]		$E_{u,\text{Max}}$ [mm]	$E_{u,\text{RMS}}$ [mm]
Centered	0.63	1.13	0.49	0.69	0.06	0.178
Line	1.27	1.53	0.26	1.37	0.10	0.160
Load	1.90	1.79	-0.11	1.83	-0.07	0.115

* Simulation results are for a center loaded inextensional curved beam with 12.9 mm radius with simulated random noise, with RMS value of $\Delta\kappa \approx 4.5 \text{ m}^{-1}$ (approximately 90% of the average curvature value of the $u_{\text{Applied}} = 0.63$ mm load case) and maximum value of $\Delta\kappa \approx 8.2 \text{ m}^{-1}$.

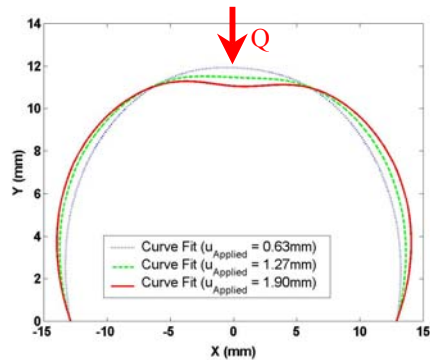


Fig. 9. Plot of reconstructed shape for centered loaded sensor based on measured curvature

shape of a deformed membrane. When moderate levels of noise are added, the maximum position error increases to as much as 10% for moderate deflections. Since it is difficult to predict the RMS noise of actual sensor data without extensive characterization, random noise was introduced to the simulation at the same order of magnitude as the widest “hysteresis gap” presented in Fig. 8. The accuracy of the surface reconstruction improves and the sensitivity to sensor noise decreases rapidly as the number of sensors increases. Of course, increasing the number of sensors also increases the difficulty in manufacturing and the computation time. For the cylindrical surface test (Table 2) the effect of noise was most significant for small deflections, where noise had a greater influence in comparison to the small curvature changes measured by the sensors.

6.2 Experimental Results

Hysteresis test: Iteration of the sensor design has led to improved performance, although mechanical hysteresis persists. Sensor data were collected to complete one hysteresis loop. The widest hysteresis gap exists for positive curvature measurements, $\Delta\kappa_{\text{Max, hysteresis}} \approx 7 \text{ m}^{-1}$. Though this is significant, it represents a three-fold improvement over the first generation design. A careful examination of the hysteresis in Fig. 8 gives some indication that the sensor is more repeatable for negative curvature readings. This may be the result of inhomogeneous bonding of strain gages to the substrate.

Centered line load test: The centered line load tests (Table 2 and Fig. 9) show that reasonable shape reconstruction can be obtained despite errors in the estimated maximum deflection, u_{Max} . The accuracy of the calculated center deflection improves as the applied deflection, u_{Applied} , increases. The influence of noise on sensor measurements becomes less significant at higher deflections, as deflection induced signals increase. Additional sensor readings should improve results.

The initial shape of the sensor was chosen to resemble robot fingertips currently used for dexterous manipulation. However, superimposing a relatively high initial curvature on the sensor may exacerbate sensor hysteresis and ultimately sensor accuracy.

Our preliminary tests with the second-generation prototype indicate that future sensors should be packaged to reduce the initial curvature, to improve sensor performance (reducing hysteretic error contributions). The feasibility of combining the sensing element and electronics on a single flexible substrate has been shown. However, our experience suggests that it is more practical to separate the sensing element from the sensor electronics while in the prototyping stage. Sensor electronics with a suitable flex circuit connector can be acquired inexpensively from commercial PCB vendors, permitting rapid independent iteration of the flexible sensing element.

The authors believe that the approach of directly sensing curvature in a compliant membrane holds promise for dexterous manipulation and telemanipulation. The resulting sensors are inexpensive and robust and can be applied to soft, curved fingertips. Estimation of local object geometry is computationally simple and sensor bandwidth is limited primarily by analog conversion time. If combined with intrinsic contact sensing (Bicchi, *et al.* 1993), it is possible to reduce conversion time by only sampling regions of interest.

7. ACKNOWLEDGEMENTS

This work is supported by the National Science Foundation under grant NSF/IIS-0099636. Special thanks are due to Dr. Herb Rauch for suggestions on the numerical analysis and tireless assistance in editing the manuscript. The authors also thank members of the Stanford Dexterous Manipulation Lab for their help and encouragement while completing this work.

8. REFERENCES

- Bicchi A, Salisbury JK, Brock DL (1993) Contact Sensing From Force Measurements. *J Robotics Research* 12(3), pp 249–262
- Brockett RW (1985) Robotic Hands with Rheological Surfaces. *IEEE ICRA Proceedings* pp 942–946
- Dario P (1991) Tactile Sensing : Technology And Applications. *Sensors And Actuators A-Physical* 26(1–3), pp. 251–256
- Lee MH (2000) Tactile sensing: New directions, new challenges. *J Robotics Research* 19(7), pp 636–643
- Ferrier NJ, Brockett RW (2000) Reconstructing The Shape of a Deformable Membrane from Image Data. *J Robotics Research* 19(9), pp 795–816
- Fraden J (1996) “Handbook of Modern Sensors.” 2nd edn. Springer-Verlag, New York
- Montana DJ (1988) The Kinematics of Contact and Grasp. *J Robotics Research* 7(3), pp 17–32
- Nowlin WC (1991) Experimental Results On Bayesian Algorithms For Interpreting Compliant Tactile Sensing Data. *IEEE ICRA Proceedings* pp 378–383
- Russell RA (1992) A Tactile Sensor Skin for Measuring Surface Contours. *IEEE TENCON* 1:pp 262–266
- Timoshenko SP, Gere JM (1961) *Theory of Elastic Stability*. McGraw-Hill, pp 340–342